analytical chemistry

pubs.acs.org/ac Letter

Nanopore-Enabled Dark-Field Digital Sensing of Nanoparticles

Vignesh Sundaresan,* Jarek Metro, Allison R Cutri, Milan Palei, Varun Mannam, Christiana Oh, Anthony J. Hoffman, Scott Howard, and Paul W. Bohn*

Cite This: https://doi.org/10.1021/acs.analchem.3c02943 Read Online

ACCESS | Metrics & More | Article Recommendations | Supporting Information

ABSTRACT: In this study, we use nanopore arrays as a platform for detecting and characterizing individual nanoparticles (NPs) in real time. Dark-field imaging of nanopores with dimensions smaller than the wavelength of light occurs under conditions where trans-illumination is blocked, while the scattered light propagates to the far-field, making it possible to identify nanopores. The intensity of scattering increases dramatically during insertion of AgNPs into empty nanopores, owing to their plasmonic properties. Thus, momentary occupation of a nanopore by a AgNP produces intensity transients that can be analyzed to reveal the following characteristics: (1) NP scattering intensity, which scales with the sixth power of the AgNP radius, shows a normal distribution arising from the heterogeneity in NP size, (2) the nanopore residence time of NPs, which was observed to be stochastic with no permselective effects, and (3) the frequency of AgNP capture events on a 21 × 21 nanopore array, which varies linearly with the concentration of the NPs, agreeing with the frequency calculated from theory. The lower limit of detection (LOD) for NPs was 130 fM, indicating that the measurement can be used in applications in which ultrasensitive detection is required. The results presented here provide valuable insights into the dynamics of NP transport into and out of nanopores and highlight the potential of nanopore arrays as powerful, massively parallel tools for nanoparticle characterization and detection.

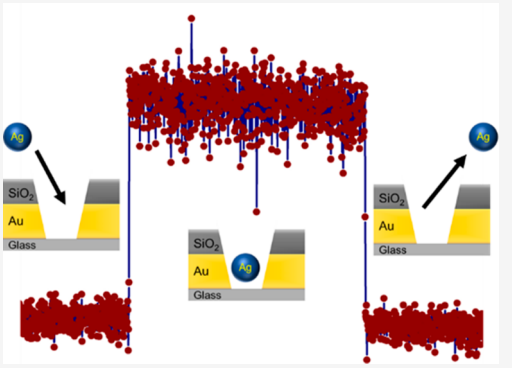

Digital sensing of nanoparticles (NPs) and NP-supported biomarkers has recently gained considerable attention due to its capacity to enhance analytical resolution and sensitivity, while also providing nearly background-free signals.[1,2] Three use cases have attracted significant attention: (1) Optical-based digital sensing methods utilize Au NPs to detect analytes, such as nucleic acids based on particle counting through dark-field microscopy, where probe DNA-functionalized Au NPs bind to target DNA and are isolated through a sandwich assay with magnetic beads.[3] The concentration of the target DNA is determined by counting the released Au NPs, with the number of particles directly corresponding to the target DNA concentration. (2) Walt and co-workers developed the single-molecule optical array (Simoa) approach to detect and quantify biomarkers by utilizing beads to implement immunoassays by encapsulating them individually in microwells.[4−7] In this approach, fluorogenic reactions are turned on only if the analyte is present in the beads or microwells, allowing the microwells containing the analyte to be identified. The analyte concentration is obtained by counting the number of strongly emitting microwells using fluorescence microscopy. (3) Finally, electrochemistry-based digital sensing is usually based on counting/quantifying surface collisions or nanoimpacts, in which single NPs stochastically collide with an ultramicroelectrode (UME) biased to a well-defined electrochemical potential.[8−11] The collision generates isolated transient current spikes or steps, which are associated with single NP collision events. This method can be employed to detect both bare NPs and biomarker-functionalized NPs.[12−14] Although these NP-based methods can provide high sensitivity, with LODs in the femtomolar concentration range, their appeal would be enhanced by making them faster and/or nondestructive.

To address the possibility of enhanced digital detection, optical dark-field microscopy is explored here to monitor the transient capture of single AgNPs in the absence of an electrochemical bias, i.e., at an open-circuit potential. We employ arrays of nanopores, fabricated to satisfy the requirements of zero-mode waveguide (ZMW) operation,[15] with pore diameters, d, smaller than a critical value, $d_c \sim \lambda/1.7$, where λ is the excitation wavelength in the medium. Under these conditions, the scattered light intensity from individual nanopores is bimodal, depending on whether or not the specific pore contains either 0 or ≥1 AgNP. The ZMW nanopore structure also facilitates the sequestration of single

Received: July 5, 2023
Accepted: August 17, 2023

NPs from the bulk and enables the acquisition of reliable scattering intensity-time readouts which narrate the NP occupation history of a given nanopore. Moreover, the array of nanopores enables massively parallel multichannel data acquisition, resulting in high-throughput analysis. After automating the counting of NP capture events from a 21 × 21 (441) nanopore array, an LOD of 130 fM was obtained for 78 nm diameter AgNPs in an acquisition lasting 75 s.

Nanopore arrays were fabricated on a Au-SiO_2 structure as previously reported by our laboratory, and a detailed procedure is provided in the Supporting Information (SI).[16−18] Using this fabrication procedure, an array of 21 × 21 nanopores (a total of 441 nanopores) with an interpore separation of 2 μm was fabricated, as shown in Figure 1A. The cross-section of an

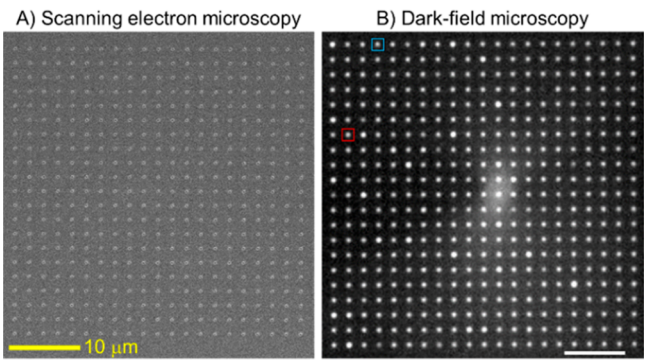

Figure 1. Images of a 21 × 21 nanopore array. (A) SEM and (B) dark-field microscopy images. Scale bars: 10 μm.

individual nanopore, shown in Figure S1, displays an inverted conical frustum with approximate top and bottom diameters of 160 and 120 nm, respectively. Next, the entire 21 × 21 nanopore array was imaged using a transmission-based dark-field microscope (DFM, Figure S2). DFM image of the nanopore array (Figure 1B) shows that it blocks the normal transmission of incident light completely; due to the ZMW character of the structure, scattered light from the nanopores is effectively out-coupled and captured in the far-field with the EM-CCD detector. The resulting image shows an array of bright spots where each bright spot corresponds to an individual nanopore.

Next, a solution containing 13 pM (7.8×10^9 particles mL^{-1}) of 78 nm diameter AgNPs was introduced to the nanopore array substrate and monitored using DFM with individual frame integration times of 50 ms. Under these conditions, the volume-based average occupancy of the individual nanopores with volume 6 aL is $\langle n_{pore} \rangle \sim 4.65 \times 10^{-5}$, and the occupancy for the entire array is $\langle n_{array} \rangle \sim 0.02$. Because the expectation occupancy of any individual nanopore is ∼0, the background signal consists of light scattered from nanopores containing only solvent. The introduction of AgNPs caused the nanopore array to exhibit blinking behavior, consisting of transient high-intensity events localized to individual nanopores, which are apparent in SI, Video 1. To analyze the blinking behavior, we used a custom MATLAB code (see SI, Section 4, Figures S3 and S4 for detailed information) to obtain background-subtracted intensities that were plotted as a function of time for each nanopore and used for further analysis.

Figure 2 shows representative intensity-time traces from two different color-coded nanopores (red and blue) in Figure 1B.

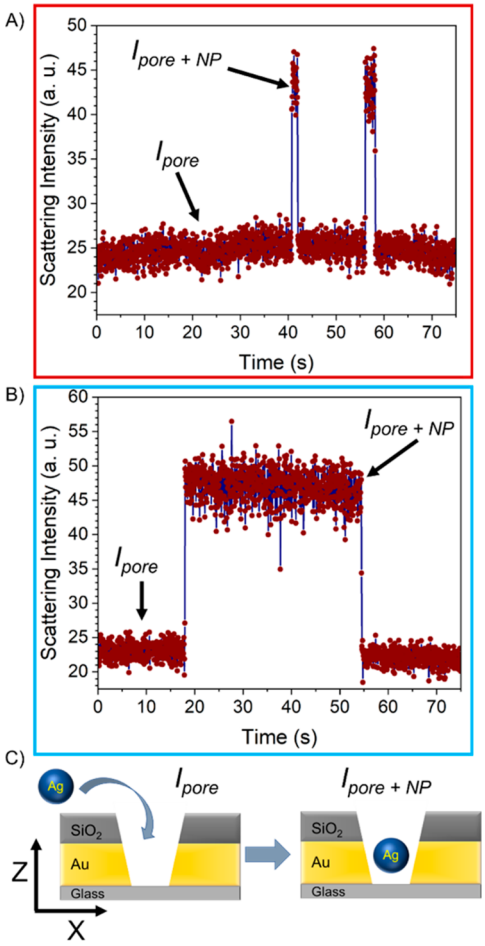

Figure 2. Nanopore scattering behavior in the presence of AgNPs. Intensity−time traces of two nanopores are shown in the (A) red and (B) blue boxes in Figure 1B. (C) Schematic diagram showing a cross-sectional view of a single nanopore before and after the insertion of AgNPs into a nanopore, causing the scattering intensity to increase from I_{pore} to $I_{pore+NP}$.

At t = 0 s, Figure 2A shows a low baseline scattering intensity I_{pore} that remains constant until ca. 40 s; this is assigned to empty nanopore scattering. Shortly after 40 s, there is a sharp increase in the intensity, assigned to $I_{pore+NP}$, which then returns back to I_{pore} after ∼1 s. Another, somewhat longer, intensity transient is observed at t = 55−58 s. Both transients exhibit essentially the same intensity increase over the baseline. We attribute both intensity transients to stochastic capture and momentary trapping of single NPs within the nanopore. As the AgNP enters the nanopore, the scattering intensity increases due to the localized surface plasmon resonance (LSPR) at the resonant wavelength of the AgNP, as shown schematically in Figure 2C. The intensity−time trace in Figure 2B shows another transient response with a much longer residence time (τ = 35 s) of the NP in the nanopore than in either of the transients in Figure 2A. Intensity−time traces of a representative selection of other nanopores are shown in Figure S5.

To better understand the coupling of LSPR modes with nanopore scattering and coupling to the far-field during AgNP insertion, finite-difference time-domain (FDTD) simulations were performed (see SI, Section 6, for details). The electric field distribution for 450 nm radiation propagating through a

https://doi.org/10.1021/acs.analchem.3c02943
Anal. Chem. XXXX, XXX, XXX−XXX

single unoccupied (i.e., no AgNP) nanopore under dark-field illumination shows that the nanopore blocks trans-illumination, and only a small portion (~8%) of the scattered light is coupled to the far-field, Figure S6A,B. However, if an 80 nm diameter AgNP is placed at the bottom of the nanopore, a dipolar plasmon mode associated with the AgNP effectively couples to the far field, Figure S6C,D. In contrast to these results, placing the AgNP at the top or middle of the nanopore structure does not produce dipolar plasmon modes at the bottom of the nanopore, as shown in Figure S7. Overall, the FDTD simulation confirms that insertion of AgNPs into the bottom of the nanopore significantly increases the scattering intensity by effectively coupling dipolar plasmon modes to the far-field.

After confirmation that the scattering intensity increase is due to the transport of AgNPs into the nanopore, the intensity behaviors were analyzed from each of the transients. The intensity increase due to the NP insertion (I_{NP}) was calculated by subtracting I_{pore} from $I_{pore+NP}$, i.e., $I_{NP} = I_{pore+NP} - I_{pore}$. Figure 3A shows a histogram of I_{NP} obtained from 1057 intensity−time traces exhibiting a normal distribution with average $\langle I_{NP} \rangle$ = 17.8 and standard deviation σ_I = 3.4. The measured value for I_{NP} depends on two factors: (1) the size of the NP and (2) the axial (z-axis) position of the NP within the nanopore. The simulations in Figures S6 and S7 show that the NP scattering is strongest when the nanoparticle is located at the bottom of the nanopore, so dispersion in the axial position is less important in determining the I_{NP} distribution in Figure 3A than dispersion in the size distribution of the nanoparticles. Assigning the I_{NP} distribution predominantly to heterogeneity in the NP radius also makes sense, because for a plasmonic NP the scattering cross-section is proportional to the sixth power of NP radius as shown in eq 1,[19,20]

$$\sigma_{scatt} = \frac{8\pi}{3} k^4 R^6 \left| \frac{\varepsilon_p - \varepsilon_m}{\varepsilon_p - 2\varepsilon_m} \right| \quad (1)$$

where σ_{scatt} is the scattering cross-section for a spherical NP, k is the wavenumber of the electric field, R is the radius of the NP, and ε_p and ε_m are the relative permittivities of the NP and surrounding medium, respectively.

Further, the distribution of experimentally observed I_{NP} values varies by 19% from the average I_{NP}, which agrees well with the width of the optical scattering cross-section area distribution (~23%) given by Mie theory (see SI, section 7, for details), thus supporting the interpretation that the deviation in the I_{NP} is due to the heterogeneity in the NP size. Additionally, the experiment was repeated employing 62 ± 5 nm diameter AgNPs and the corresponding I_{NP} was analyzed. The histogram of 62 nm AgNPs I_{NP} (Figure S8, blue) shows a smaller average I_{NP} (10.9) in comparison with the I_{NP} of 78 nm diameter AgNPs (17.8), as expected based on eq 1.

Next, the AgNP residence times (τ) within the nanopore were characterized by analyzing the widths of the $I_{pore+NP}$ transients. The histogram of τ values collected from 1057 intensity−time traces shown in Figure 3B exhibits an exponential distribution with a decay constant, τ, of 8.6 s and a median τ of 2.7 s. 62% (655) of the 1057 traces analyzed showed τ less than 5 s, and 76% (802) showed τ less than 10 s. Since the NP is functionalized with citrate, while the nanopore is unfunctionalized, the variation in τ likely arises from a combination of factors: heterogeneity in the NP zeta-potential, surface charge of the nanopore, and the hindered subdiffusive motion of the NP within the confined nanopore environment. Interestingly, no permselective behavior was observed. The negatively charged SiO_2 nanopore surfaces did not significantly impede the transport of the citrate-capped AgNPs even without additional supporting electrolyte to screen the SiO_2 surface charge,[21,22] reflecting relatively small or negligible electrostatic interactions between the NP and the nanopore. Alternatively, when the Au portion of the nanopore was functionalized with biotinylated thiol, and streptavidin-functionalized 60 nm diameter AgNPs were introduced (SI, section 9), τ values as long as ~325 s, Figure S9A, nearly 40× longer than those observed for citrate-capped AgNPs. The increase in τ reflects the strong affinity between the biotin-functionalized nanopore and streptavidin-functionalized AgNPs and the effective capture/trapping of the AgNPs.

Next, we calculated the experimental frequency (f_{exp}) of AgNP (concentration = 13 pM) intensity transients on a 21 × 21 array nanopore. In 75 s, 141.8 events were observed on average over three separate experiments, which corresponds to f_{exp} = 1.89 s^{-1}. The theoretical frequency (f_{th}) of AgNPs entering the recessed nanopore structure was calculated using the following equation,[23]

$$f_{th} = \frac{4\pi C_{NP} D_{NP} r^2 N_A N_{pore}}{4L + \pi r} \quad (2)$$

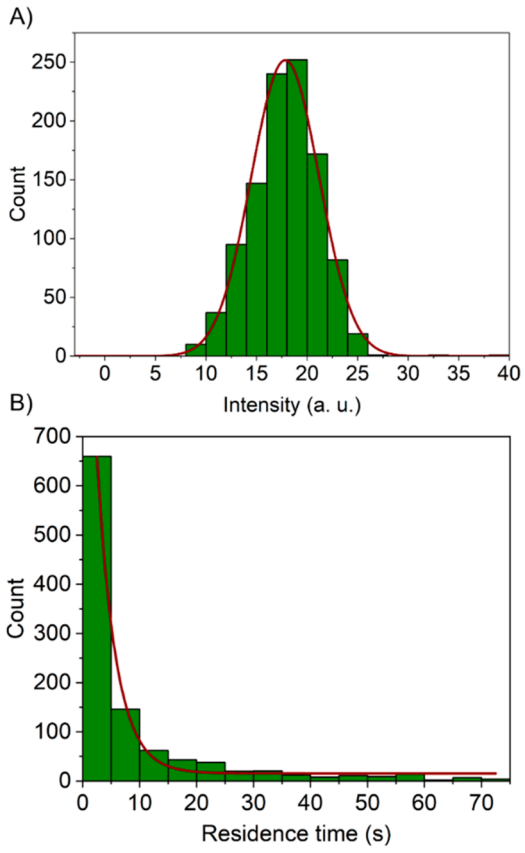

Figure 3. Experimental scattering intensity and residence time distributions for AgNPs in nanopores. (A) NP scattering intensity (I_{NP}) histogram with a fit to a normal distribution (red solid line). (B) NP residence time (τ) histogram with a fit to an exponential function (red solid line). Both histograms were created by analyzing 1057 intensity−time traces.

https://doi.org/10.1021/acs.analchem.3c02943
Anal. Chem. XXXX, XXX, XXX−XXX

where C_{NP} is the NP concentration, D_{NP} is the NP diffusion coefficient, r is the radius of the nanopore, L is the length of the nanopore, N_A is the Avogadro's number, and N_{pore} is the number of nanopores in the array. It is important to note that eq 2 is strictly true for recessed cylindrical structures with uniform radius, and the nanopores used here were conical frustum-shaped with different top and bottom diameters. Nevertheless, the nanopores were approximated as being cylindrical with $r \sim 100$ nm, for which a 13 pM AgNP concentration produces a calculated $f_{th} = 1.56$, which agrees reasonably well with the experimental value $f_{exp} = 1.89 \pm 0.12$. The experiment was then repeated with different concentrations of AgNPs, and the observed total number capture events show a linear increase with AgNP concentration, as expected, Figure 4. The lowest detectable concentration was

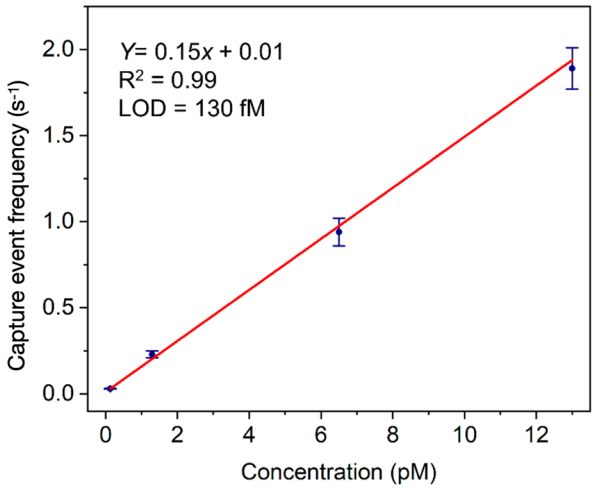

Figure 4. Capture event frequency as a function of AgNP concentration (13, 6.5, 1.3, and 0.13 pM) with a linear fit shown as a red solid line.

0.13 pM which produced 2.3 capture events on average from three 75 s-duration experiments. The values of f_{exp} and f_{th} (Table S1) show reasonable agreement for all concentrations of 0.13 pM $\leq C \leq$ 13 pM.

In conclusion, optical dark-field scattering has been used to investigate the transient capture of individual AgNPs on a 21 × 21 nm array with pore diameters smaller than the wavelength of visible light. The intensity−time traces of individual NP capture events indicate that the scattering intensity increases dramatically upon insertion of NPs into the nanopore, with scattering being much stronger for NPs near the bottom of the pore, a result confirmed by FDTD simulations. The NP-induced scattering intensities exhibit a normal distribution, which tracks the NP size distribution, and the residence time of the citrate-terminated AgNPs in the nanopore is stochastic. Designing the NP surfaces to be chemically complementary to the internal nanopore surfaces produced capture and trapping of individual NPs. Moreover, the frequency of capture events is linear with AgNP concentration, in excellent agreement with the theoretical frequency with 130 fM being the lowest detectable NP concentration. The nanopore scattering approach developed in this study provides a valuable method for isolating and efficiently examining numerous individual NPs in a highly parallel platform. Furthermore, although not explored here, the gold optical cladding layer can be used as a working electrode, enabling high-throughput correlated optical-electrochemical measurements of single NPs. Lastly, the nanopores can be functionalized with biorecognition elements, enabling the detection of biomarker-tagged NPs, thus, accessing a wide range of diagnostically useful determinations.

■ ASSOCIATED CONTENT

Supporting Information

The Supporting Information is available free of charge at https://pubs.acs.org/doi/10.1021/acs.analchem.3c02943.

Chemical and materials, fabrication of nanopore array, dark-field imaging experimental setup, the process of analyzing image stacks through MATLAB, additional intensity-time traces with intensity transients, FDTD simulation details, scattering intensity histogram for 78 and 62 nm AgNPs, and residence time analysis for biotin functionalized nanopore and streptavidin labeled AgNPs (PDF)

Video showing the dynamic capture of single nanoparticles in the nanopores. Video recorded at 20 fps and displayed at 200 fps (AVI)

■ AUTHOR INFORMATION

Corresponding Authors

Vignesh Sundaresan − *Department of Chemistry and Biochemistry, University of Mississippi, University, Mississippi 38655, United States;* orcid.org/0000-0001-9390-1681; Email: vsundare@olemiss.edu

Paul W. Bohn − *Department of Chemistry and Biochemistry, University of Notre Dame, Notre Dame, Indiana 46556, United States; Department of Chemical and Biomolecular Engineering, University of Notre Dame, Notre Dame, Indiana 46556, United States;* orcid.org/0000-0001-9052-0349; Email: pbohn@nd.edu

Authors

Jarek Metro − *Department of Chemistry and Biochemistry, University of Notre Dame, Notre Dame, Indiana 46556, United States;* orcid.org/0000-0002-3687-0417

Allison R Cutri − *Department of Chemistry and Biochemistry, University of Notre Dame, Notre Dame, Indiana 46556, United States*

Milan Palei − *Department of Electrical Engineering, University of Notre Dame, Notre Dame, Indiana 46556, United States;* orcid.org/0000-0003-4387-5184

Varun Mannam − *Department of Electrical Engineering, University of Notre Dame, Notre Dame, Indiana 46556, United States*

Christiana Oh − *Department of Chemical and Biomolecular Engineering, University of Notre Dame, Notre Dame, Indiana 46556, United States;* orcid.org/0000-0002-6018-920X

Anthony J. Hoffman − *Department of Electrical Engineering, University of Notre Dame, Notre Dame, Indiana 46556, United States*

Scott Howard − *Department of Electrical Engineering, University of Notre Dame, Notre Dame, Indiana 46556, United States;* orcid.org/0000-0003-3246-6799

Complete contact information is available at: https://pubs.acs.org/10.1021/acs.analchem.3c02943

Notes

The authors declare no competing financial interest.

https://doi.org/10.1021/acs.analchem.3c02943
Anal. Chem. XXXX, XXX, XXX−XXX

■ ACKNOWLEDGMENTS

This work was supported by the National Science Foundation through Grant NSF2303574 and by the University of Notre Dame through the Faculty Research Support Program − Initiation Grant. The authors thank the University of Notre Dame Nanofabrication Facility and Notre Dame Integrated Imaging Facility for their assistance with materials fabrication and characterization.

■ REFERENCES

(1) Krainer, G.; Saar, K. L.; Arter, W. E.; Welsh, T. J.; Czekalska, M. A.; Jacquat, R. P. B.; Peter, Q.; Traberg, W. C.; Pujari, A.; Jayaram, A. K.; Challa, P.; Taylor, C. G.; van der Linden, L.-M.; Franzmann, T.; Owens, R. M.; Alberti, S.; Klenerman, D.; Knowles, T. P. J *Nat. Commun.* **2023**, *14* (1), 653.
(2) Cretich, M.; Daaboul, G. G.; Sola, L.; Ünlü, M. S.; Chiari, M. *Trends Biotechnol.* **2015**, *33* (6), 343−351.
(3) Li, T.; Xu, X.; Zhang, G.; Lin, R.; Chen, Y.; Li, C.; Liu, F.; Li, N. *Anal. Chem.* **2016**, *88* (8), 4188−4191.
(4) Rissin, D. M.; Kan, C. W.; Campbell, T. G.; Howes, S. C.; Fournier, D. R.; Song, L.; Piech, T.; Patel, P. P.; Chang, L.; Rivnak, A. J.; Ferrell, E. P.; Randall, J. D.; Provuncher, G. K.; Walt, D. R.; Duffy, D. C. *Nat. Biotechnol.* **2010**, *28* (6), 595−599.
(5) Wu, C.; Maley, A. M.; Walt, D. R. *Crit. Rev. Clin. Lab. Sci.* **2020**, *57* (4), 270−290.
(6) Gilboa, T.; Cohen, L.; Cheng, C.-A.; Lazarovits, R.; Uwamanzu-Nna, A.; Han, I.; Griswold, K., Jr.; Barry, N.; Thompson, D. B.; Kohman, R. E.; Woolley, A. E.; Karlson, E. W.; Walt, D. R. *Angew. Chem., Int. Ed.* **2021**, *60* (49), 25966−25972.
(7) Wu, C.; Dougan, T. J.; Walt, D. R. *ACS Nano* **2022**, *16* (1), 1025−1035.
(8) Xu, W.; Zou, G.; Hou, H.; Ji, X. *Small* **2019**, *15* (32), 1804908.
(9) Defnet, P. A.; Anderson, T. J.; Zhang, B. *Curr. Opin. Electrochem.* **2020**, *22*, 129−135.
(10) Stevenson, K. J.; Tschulik, K. A. *Curr. Opin. Electrochem.* **2017**, *6* (1), 38−45.
(11) Glasscott, M. W.; Dick, J. E. *Anal. Chem.* **2018**, *90* (13), 7804−7808.
(12) Sekretareva, A. *Sensors and Actuators Reports* **2021**, *3*, 100037.
(13) Qiu, X.; Tang, H.; Dong, J.; Wang, C.; Li, Y. *Anal. Chem.* **2022**, *94* (23), 8202−8208.
(14) Dick, J. E.; Hilterbrand, A. T.; Strawsine, L. M.; Upton, J. W.; Bard, A. J. *Proc. Natl. Acad. Sci. U. S. A.* **2016**, *113* (23), 6403−6408.
(15) Levene, M. J.; Korlach, J.; Turner, S. W.; Foquet, M.; Craighead, H. G.; Webb, W. W. *Science* **2003**, *299* (5607), 682−686.
(16) Sundaresan, V.; Bohn, P. W. *Chem. Sci.* **2020**, *11* (40), 10951−10958.
(17) Baek, S.; Han, D.; Kwon, S.-R.; Sundaresan, V.; Bohn, P. W. *Anal. Chem.* **2022**, *94* (9), 3970−3977.
(18) Baek, S.; Cutri, A. R.; Han, D.; Kwon, S.-R.; Reitemeier, J.; Sundaresan, V.; Bohn, P. W. *J. Appl. Phys.* **2022**, *132* (17), 174501.
(19) van Dijk, M. A.; Tchebotareva, A. L.; Orrit, M.; Lippitz, M.; Berciaud, S.; Lasne, D.; Cognet, L.; Lounis, B. *Phys. Chem. Chem. Phys.* **2006**, *8* (30), 3486−3495.
(20) Tcherniak, A.; Ha, J. W.; Dominguez-Medina, S.; Slaughter, L. S.; Link, S. *Nano Lett.* **2010**, *10* (4), 1398−1404.
(21) Fu, K.; Bohn, P. W. *ACS Cent. Sci.* **2018**, *4* (1), 20−29.
(22) Fu, K.; Han, D.; Crouch, G. M.; Kwon, S.-R.; Bohn, P. W. *Small* **2018**, *14* (18), 1703248.
(23) Arrigan, D. W. M. *Analyst* **2004**, *129* (12), 1157−1165.

https://doi.org/10.1021/acs.analchem.3c02943
Anal. Chem. XXXX, XXX, XXX−XXX